

Article

2D Temperature Analysis of Energy and Exergy Characteristics of Laminar Steady Flow across a Square Cylinder under Strong Blockage

M. Ozgun Korukcu

Department of Mechanical Engineering, University of Uludag, Gorukle, 16059 Bursa, Turkey;
E-Mail: ozkorukcu@uludag.edu.tr; Tel.: +90-224-2941927; Fax: +90-224-2941903

Academic Editor: Marc A. Rosen

Received: 10 March 2015 / Accepted: 7 May 2015 / Published: 12 May 2015

Abstract: Energy and exergy characteristics of a square cylinder (SC) in confined flow are investigated computationally by numerically handling the steady-state continuity, Navier-Stokes and energy equations in the Reynolds number range of $Re = 10-50$, where the blockage ratio ($\beta = B/H$) is kept constant at the high level of $\beta = 0.8$. Computations indicated for the upstream region that, the mean non-dimensional streamwise (u/U_o) and spanwise (v/U_o) velocities attain the values of $u/U_o = 0.840 \rightarrow 0.879$ and $v/U_o = 0.236 \rightarrow 0.386$ ($Re = 10 \rightarrow 50$) on the front-surface of the SC, implying that Reynolds number and blockage have stronger impact on the spanwise momentum activity. It is determined that flows with high Reynolds number interact with the front-surface of the SC developing thinner thermal boundary layers and greater temperature gradients, which promotes the thermal entropy generation values as well. The strict guidance of the throat, not only resulted in the fully developed flow character, but also imposed additional cooling; such that the analysis pointed out the drop of duct wall ($y = 0.025$ m) non-dimensional temperature values (ζ) from $\zeta = 0.387 \rightarrow 0.926$ ($Re = 10 \rightarrow 50$) at $x_{th} = 0$ mm to $\zeta = 0.002 \rightarrow 0.266$ at $x_{th} = 40$ mm. In the downstream region, spanwise thermal disturbances are evaluated to be most inspectable in the vortex driven region, where the temperature values show decrease trends in the spanwise direction. In the corresponding domain, exergy destruction is determined to grow with Reynolds number and decrease in the streamwise direction ($x_{ds} = 0 \rightarrow 10$ mm). Besides, asymmetric entropy distributions as well were recorded due to the comprehensive mixing caused by the vortex system.

Keywords: confined-flow; momentum; thermal; entropy generation

1. Introduction

Over the last few decades, the flow past bluff bodies has been the subject of quite a number of researches. Most of these studies were focused on circular cylinders [1] and provided a substantial scientific documentation; however, momentum and thermal mechanisms around square cylinders (SC) have not been studied in detail to the same extent. Among the available literature on SCs, as some of them were focused on unconfined free-stream fluid flows [2–6], in others the SC is introduced into a channel flow to enhance mixing and heat transfer [6–15]. In addition to the academic concern, this type of flow is of relevance for many practical applications, such as buildings, bridges, towers, electronic cooling and heat exchangers. Besides the flow and heat transfer characteristics, being the main concerns of internal flow applications, investigations into viscous effects, velocity and temperature profiles as well constitute a wide research area due to their direct role in the entropy generation of thermo-fluid systems. Thus, studies on second-law characteristics have recently been the topic of great interest in various fields such as combustion processes [16] and fuel cells [17].

Lately, remarkable scientific efforts have been devoted to research on the momentum and heat transfer mechanisms of SCs immersed in fluids, due to the practical and fundamental significance of the subject matter. Nirmalkar *et al.* [2] considered the regime to be steady up to $Re_{cr} = 40$ in the unconfined flow case. They examined the velocity and shear rate profiles along the center planes in detail, to identify the impact of Reynolds number on the yielded (fluid-like) and the unyielded (solid-like) regions. In another computational study with unconfined flow, Rao *et al.* [3] established the critical Reynolds number for the onset of vortex instability in the downstream region as $Re_{cr} = 45$. Dhiman *et al.* [4] researched in the narrow Reynolds number range of $Re = 1–30$ for the unconfined flow. They essentially discussed the complex flow field, especially in the rear of the SC, through detailed streamline and isotherm contour presentations. Momentum characteristics of a porous SC was also included in the unconfined flow investigations by Chen *et al.* [5], who evaluated similar downstream vortex generation in the steady limits of $Re = 2–40$. Sharma and Eswaran [6] studied the very weak blockage case of $\beta = 0.05$; similar to [2] they as well determined the stability limit as $Re_{cr} = 40$ and reported longer recirculation zones and lower drag forces with Reynolds number for the steady flow regime. Chatterjee and Mondal [7] as well reported similar variations in momentum and heat transfer characteristics with Reynolds number in the same blockage ratio of $\beta = 0.05$. Momentum and heat transfer characteristics of a SC in confined flow ($\beta = 1/15$) was numerically investigated by Paliwal *et al.* [8]; who evaluated the variation of recirculation length (L_R), drag coefficient (C_D) and Nusselt number (Nu) in the Reynolds number and power law index ranges of $Re = 5–40$ and $n = 0.5–1.4$. Sen *et al.* [9], by employing a stabilized finite-element formulation to discretize the equations of incompressible fluid flow in two-dimensions, presented for the flow past a stationary SC at zero incidence for Reynolds numbers up to $Re = 150$. They derived equations for the variation of L_R , C_D and angle of separation (θ_s) with Reynolds number for the fixed blockage ratio case of $\beta = 0.01$. At the blockage ratio of $\beta = 1/8$, Breuer *et al.* [10] carried out fluid mechanics investigations with the maximum Reynolds number of $Re = 300$. They determined that the downstream fluctuations were suppressed by the channel walls up to the critical value of $Re_{cr} = 60$, causing the flow to settle in the steady regime. They supported their findings on L_R and C_D with velocity profiles of the upstream and downstream regions. Bouaziz *et al.* [11] as well considered the confined flow with $\beta = 1/8$. For the

high Prandtl number of $Pr = 50$, they worked in the Reynolds number range of $Re = 20\text{--}200$, comprising both steady and unsteady flows. Dhiman *et al.* [12] aimed to explore the buoyancy effects at the blockage ratio of $\beta = 1/8$ for the Reynolds number range of $Re = 1\text{--}30$. Despite the magnitude of the numerical values, they evaluated similar variation trends in the momentum and thermal characteristics with Reynolds number in the presence of buoyancy. Steady and unsteady laminar flows past a heated SC were numerically investigated by Rahnama and Hadi [13] for the blockage ratio of $\beta = 1/8$ and with the Reynolds numbers up to 200. They showed a nearly linear increase in recirculation length and decrease in drag coefficient with increasing Reynolds number for the steady flow regime; and an increase in the total Nusselt number and drag coefficient with a Reynolds number for unsteady flow regime. Dhiman *et al.* [14] performed steady fluid mechanics computations in the blockage ratio range of $\beta = 1/8\text{--}1/4$ and set the upper stability limit for these confined flow scenarios in terms of Reynolds number as $Re = 45$. They affirmed that the length of the recirculation zone linearly increases with the Reynolds number and decreases with blockage ratio. Sharma and Eswaran [15] examined the flow and heat transfer characteristics in confined flow for the wide Reynolds number and blockage ratio ranges of $Re = 50\text{--}150$ and $\beta = 0.1\text{--}0.5$. They announced that the flow with $Re = 50$ becomes steady for $\beta \geq 0.2$; they additionally exhibited the front, top and back face Nusselt numbers for each Reynolds number case explicitly and clarified their correspondence with the momentum mechanisms.

Due to its potential in describing the overall system performance, second-law analysis and entropy generation based investigations, on internal fluid flow related problems, have recently been considered as not only a scientific but also a technologic requirement. Hooman and Haji [18] carried out a numerical study to interpret the entropy generation characteristics for a thermally developing forced convection problem in a rectangular duct with isoflux walls. They presented their findings as a function of the longitudinal coordinate, the aspect ratio and Brinkman number; and established that as the heat transfer mechanisms grow with Brinkman number, the contrary is valid for the entropy generation values. As Zimparov [19] reviewed passive heat transfer augmentation techniques for single-phase flows, Chen and Du [20] investigated the effects of thermal Rayleigh number, ratio of buoyancy forces and aspect ratio on entropy generation of turbulent double-diffusive natural convection in a rectangle cavity. Rakshit and Balaji [21] reported the results of a numerical investigation of conjugate convection from a finned channel, where the vertical rectangular fins were mounted outside the horizontal channel. Laminar forced convection and entropy generation in a helical coil with constant wall heat flux was numerically investigated by Ko [22]. He suggested that the optimal Reynolds number is to be chosen according to the flow operating condition so that the thermal system can have the least irreversibility and best exergy utilization. In a supplementary work, Guo *et al.* [23] investigated the impact of duct curvature on the second law characteristics and determined the entropy generation to decrease with curvature ratio at the same Reynolds number. For the flow of a variable-viscosity fluid through a channel with a non-uniform wall temperature, Makinde [24] as well worked numerically and discussed his findings through the same parameters. Nourollahi *et al.* [25] numerically solved Navier-Stokes and energy equations to analyze the mixed convection and entropy generation in Poiseuille-Benard channel flow. They recorded that the entropy generation due to heat transfer is localized at areas where heat exchanged between the walls and the flow is maximum, while the entropy generation due to fluid friction is maximum at areas where the

velocity gradients are maximum such as vortex centers. The second law characteristics of fluid flow and heat transfer inside a circular duct under fully developed forced convection for non-Newtonian fluids are studied by Mahmud and Fraser [26], who presented their outputs through the spatial distributions of local and average entropy generation number, irreversibility ratio and Bejan number. Kurtbas *et al.* [27] discussed the heat and exergy transfer characteristics of forced convection flow through a horizontal rectangular channel with foams through the parametric values of mean exergy transfer, Nusselt number and friction factor as functions of Reynolds number. In a second-law study on the 2D laminar channel flow of incompressible viscous fluids, Kamish and Oztop [28] used the dimensionless entropy generation number to interpret the relative importance of friction to conduction by varying irreversibility distribution ratio. They additionally observed that the minimum entropy generation occurs at the location of the minimum temperature gradient in transverse direction. As Jarunghammachote [29] reported the variation of entropy generation with heat flux and duct dimensions in a hexagonal duct, Andreozzi *et al.* [30] analyzed entropy generation rates based on the velocity and temperature data of the natural convection phenomena in a vertical channel. Kotas *et al.* [31] indicated that for calculating loss of exergy, or process irreversibility, an exergy balance or the Gouy-Stodola theorem can be used. Bianco *et al.* [32,33] made a parametric study of entropy generation of nanofluid turbulent convection inside a circular tube under constant wall heat flux and wall temperature conditions. Mkwizu and Makinde [34] investigated the entropy generation in a variable viscosity channel flow of nanofluids with convective cooling. Eegunjobi and Makinde [35] investigated entropy generation in transient variable viscosity Couette flow between two concentric pipes.

Although the available literature offers a set of thermo-fluid researches of confined square cylinders, they are limited to either fluid flow or fluid flow and heat transfer; besides the researchers mostly focused on confined cases with low blockage ratio. On the other hand, in spite of the several existing investigations on second-law analysis for internal flows, entropy generation mechanisms of confined bluff bodies are not yet considered. Even though the heat transfer rates are significantly characterized by the fluid flow and boundary layer development, and the second-law mechanisms by those of the hydrodynamic and thermal behaviors, the open literature cannot offer any publication studying the linkage of the momentum-thermal values with the second-law performances of confined square cylinders. The present numerical work aims to develop a complete overview on the energy and exergy analysis of steady laminar confined flows across square cylinders for the Reynolds number range of $Re = 10-50$ at the blockage ratio of $\beta = 0.8$. Findings on momentum and thermal actions are discussed through streamlines, velocity and temperature profiles, temperature contours and temperature gradients. Results of the exergy analysis are presented by way of entropy profiles, thermal, frictional and overall entropy generation rates and Bejan numbers. Autonomous discussions are documented for the upstream, throat and downstream sections of the flow domain; but cross-debates are as well prepared to clarify the transport of the properties and the triggering influences of the neighboring domains in the flow direction. By obtaining velocity and temperature values in the flow field, entropy generation of the system was calculated. Entropy profiles indicate where the energy losses are significant and need improvements. Present study gives clear results for both frictional and temperature based entropy generation values and also for the total entropy generation values.

2. Theoretical Background

2.1. Geometry and Boundary Conditions

Figure 1 displays the geometry and the dimensions of the current analysis. As shown in Figure 1a, the SC is placed in the channel between two adiabatic walls and the distance between the center of the SC to the upper and lower walls is $H/2$. No slip boundary conditions ($u = v = 0$) are applied on the SC and the channel walls. The surfaces of the SC are held at the constant temperature T_s . Inlet temperature of the air is taken as T_{∞} , and the air enters the channel with a fully developed laminar velocity profile of $u(y) = U_c \left[1 - \left(\frac{2y}{H} \right)^2 \right]$, where U_c is the centerline velocity of the air at the channel inlet. Additionally, Figure 1b displays the geometric notation, adapted for the energy and exergy investigations. Throughout the work, the edge of the square cylinder and channel height are kept fixed to $B = 0.04$ m and $H = 0.05$ m, respectively, aiming to perform the overall computational investigations with the strong blockage condition of $\beta (=B/H) = 0.8$.

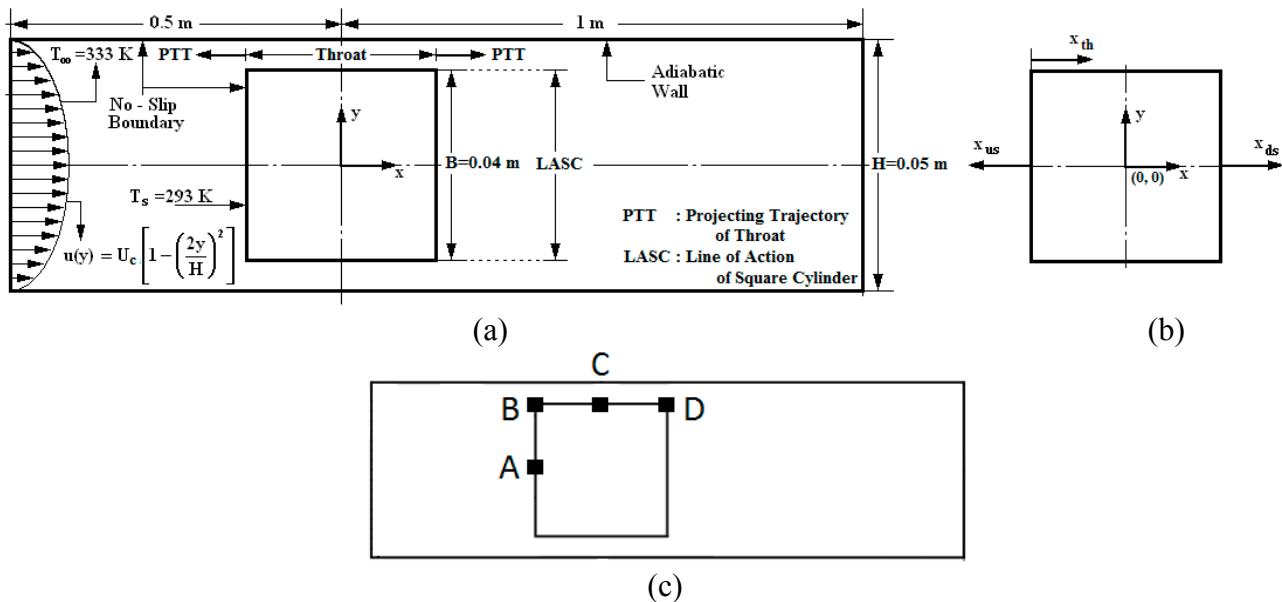


Figure 1. (a) Flow domain around the square cylinder, (b) the coordinate system, (c) control points for grid independency.

Sharma and Eswaran [6] reported, for the very weak blockage case of $\beta = 0.05$, the stability limit as $Re_{cr} = 40$. For the mild blockage ratio of $\beta = 1/8$, the downstream fluctuations were evaluated to be suppressed by the channel walls up to the critical value of $Re_{cr} = 60$ by Breuer *et al.* [10]. In the blockage ratio range of $\beta = 1/8-1/4$, Dhiman *et al.* [14] set the upper stability limit as $Re_{cr} = 45$. For the different Reynolds number and blockage ratios of $Re = 50-150$ and $\beta = 0.1-0.5$, Sharma and Eswaran [15] showed that the flow with $Re_{cr} = 50$ becomes steady for $\beta \geq 0.2$. Since the focus of the present work is to investigate the laminar boundary layer development, energy and exergy characteristics of SCs in confined flows, the computational analysis are carried out in the SC edge (B) based Reynolds number range of $Re_B = 10-50$, which is consistent with the critical Reynolds numbers reported in the steady-laminar SC investigations [6,10,14,15].

2.2. Governing Equations and Grid Independency

Besides, by simultaneously considering the traditional channel flow critical Reynolds number of $Re = 2300$ [36], for the blockage ratio and channel height of $\beta = 0.8$ and $H = 50$ mm (Figure 1a), the consequent Reynolds number for the channel flow becomes $Re_{ch} = 100$. Being compatible with these definitions, the fluid flow and heat transfer section of the present problem is structured on incompressible and constant fluid and thermal property characteristics and carried out in steady ($\frac{\partial}{\partial t} = 0$) and two-dimensional fluid domain. Under these conditions, equations governing the two-dimensional steady laminar flow are given in the master Cartesian coordinate system as

Continuity:

$$\frac{\partial u}{\partial x} + \frac{\partial v}{\partial y} = 0 \quad (1)$$

Momentum:

$$\rho \left(u \frac{\partial u}{\partial x} + v \frac{\partial u}{\partial y} \right) = -\frac{\partial P}{\partial x} + \mu \left(\frac{\partial^2 u}{\partial x^2} + \frac{\partial^2 u}{\partial y^2} \right) \quad (2)$$

$$\rho \left(u \frac{\partial v}{\partial x} + v \frac{\partial v}{\partial y} \right) = -\frac{\partial P}{\partial y} + \mu \left(\frac{\partial^2 v}{\partial x^2} + \frac{\partial^2 v}{\partial y^2} \right) \quad (3)$$

Energy:

$$u \frac{\partial T}{\partial x} + v \frac{\partial T}{\partial y} = \alpha \left(\frac{\partial^2 T}{\partial x^2} + \frac{\partial^2 T}{\partial y^2} \right) \quad (4)$$

Dimensionless form of governing equations are [37]

Continuity:

$$\frac{\partial u_*}{\partial x_*} + \frac{\partial v_*}{\partial y_*} = 0 \quad (5)$$

Momentum:

$$u_* \frac{\partial u_*}{\partial x_*} + v_* \frac{\partial u_*}{\partial y_*} = -\frac{\partial P_*}{\partial x_*} + \frac{1}{Re} \left(\frac{\partial^2 u_*}{\partial x_*^2} + \frac{\partial^2 u_*}{\partial y_*^2} \right) \quad (6)$$

$$u_* \frac{\partial v_*}{\partial x_*} + v_* \frac{\partial v_*}{\partial y_*} = -\frac{\partial P_*}{\partial y_*} + \frac{1}{Re} \left(\frac{\partial^2 v_*}{\partial x_*^2} + \frac{\partial^2 v_*}{\partial y_*^2} \right) \quad (7)$$

Energy:

$$u_* \frac{\partial \zeta}{\partial x_*} + v_* \frac{\partial \zeta}{\partial y_*} = \frac{1}{RePr} \left(\frac{\partial^2 \zeta}{\partial x_*^2} + \frac{\partial^2 \zeta}{\partial y_*^2} \right) \quad (8)$$

In addition to obtaining fluid flow and heat transfer based energy characteristics of the problem, the second-law analysis and entropy generation mechanisms are also investigated. Due to the exchange of energy and momentum between fluid and solid boundaries, entropy generates in the flow field. Local volumetric entropy generation (S''') can be calculated after the velocity and temperature fields are numerically determined. The total local entropy generation in the flow field contains thermal ($S''_{\Delta T}$) and frictional ($S''_{\Delta P}$) components [38,39]:

$$S''' = \frac{\kappa_f}{T^2} \left[\left(\frac{\partial T}{\partial x} \right)^2 + \left(\frac{\partial T}{\partial y} \right)^2 \right] + \frac{\mu}{T} \left\{ 2 \left(\frac{\partial u}{\partial x} \right)^2 + 2 \left(\frac{\partial v}{\partial y} \right)^2 + \left[\left(\frac{\partial u}{\partial y} \right) + \left(\frac{\partial v}{\partial x} \right) \right]^2 \right\} \quad (9)$$

where the thermal entropy generation is:

$$S'''_{\Delta T} = \frac{\kappa_f}{T^2} \left[\left(\frac{\partial T}{\partial x} \right)^2 + \left(\frac{\partial T}{\partial y} \right)^2 \right] \quad (10)$$

and the frictional entropy generation:

$$S'''_{\Delta P} = \frac{\mu}{T} \left\{ 2 \left(\frac{\partial u}{\partial x} \right)^2 + 2 \left(\frac{\partial v}{\partial y} \right)^2 + \left[\left(\frac{\partial u}{\partial y} \right) + \left(\frac{\partial v}{\partial x} \right) \right]^2 \right\} \quad (11)$$

and dimensionless entropy generation [40]:

$$N_s = \left[\left(\frac{\partial \zeta}{\partial x_*} \right)^2 + \left(\frac{\partial \zeta}{\partial y_*} \right)^2 \right] + \frac{Br}{\theta} \left\{ 2 \left(\frac{\partial u_*}{\partial x_*} \right)^2 + 2 \left(\frac{\partial v_*}{\partial y_*} \right)^2 + \left[\left(\frac{\partial u_*}{\partial y_*} \right) + \left(\frac{\partial v_*}{\partial x_*} \right) \right]^2 \right\} \quad (12)$$

The Bejan number *Be*, which compares the entropy generation due to the heat transfer with the total entropy generation, is defined by

$$Be = \frac{S'''_{\Delta T}}{S'''} = \frac{N_{s\Delta T}}{N_{s\Delta T} + N_{s\Delta P}} \quad (13)$$

If $Be > 1/2$, the heat transfer irreversibility dominates, for $Be < 1/2$ the fluid frictional irreversibility dominates. For $Be \cong 1/2$, entropy due the heat transfer irreversibility is comparable with the fluid frictional irreversibility.

Not only to describe the flow type and identify the considered scenarios but also to interpret the evaluated outputs in common scientific notation, the following dimensionless variables and parameters are used:

$$x_* = \frac{x}{B}; y_* = \frac{y}{H}; u_* = \frac{U}{U_c}; v_* = \frac{V}{U_c}; P_* = \frac{P}{\rho U_c^2} \quad (14 \text{ a-e})$$

$$\beta = \frac{B}{H}; Re_B = \frac{\rho U_c B}{\mu}; Pr = \frac{\mu}{\rho \alpha}; \rho = \frac{P}{RT}; Br = \frac{\mu U_c^2}{K_f(T_\infty - T_s)} \quad (15 \text{ a-e})$$

$$\theta = \frac{T_\infty - T_s}{T_s}; U_o = \frac{\int_{-H/2}^{H/2} u(y) dy}{H}; \dot{m} = \rho U_o A; \zeta = \frac{T - T_s}{T_\infty - T_s} \quad (16 \text{ a-d})$$

where x_* and y_* are non-dimensional streamwise and spanwise distances, u_* and v_* are non-dimensional streamwise and spanwise velocities, P_* is the non-dimensional pressure, β is the blockage ratio, Re_B is the SC edge based Reynolds number, Pr is the Prandtl number, ρ is the density of air, Br is the Brinkman number, θ is the non-dimensional temperature parameter, U_o is the mean velocity, \dot{m} is the mass flow rate and ζ is the non-dimensional temperature.

Fluid flow and heat transfer simulations are performed with ANSYS-CFX v14.0 (ANSYS, Cecil Township, PA, USA) [41]. ANSYS-CFX applies the element-based finite-volume method and scalably adopts the multigrid solver to the defined flow domain. For the complete set of scenarios investigated, a convergence criterion of 1×10^{-7} is used to certain negligibly small iteration errors.

For the grid independency, four different grids were investigated and pressure (P), wall shear stress (τ), velocity gradient (du/dy) and wall heat transfer coefficient (h) values from A, B, C, D points that were presented in Figure 1c were controlled and the grid independency was obtained. To get more

accurate results, the calculations were held under the grid which has 2,618,046 elements. In Table 1, values for grid independency are presented.

Table 1. Grid independency results.

	644,436 elements				1,188,596 elements			
	A	B	C	D	A	B	C	D
$P(\text{N/m}^2)$	0.0232	0.0201	9.72×10^{-3}	-9.72×10^{-4}	0.0233	0.0205	9.77×10^{-3}	-1.19×10^{-3}
$\tau(\text{N/m}^2)$	1.92×10^{-10}	8.11×10^{-3}	1.13×10^{-3}	2.54×10^{-3}	8.33×10^{-11}	9.10×10^{-3}	1.13×10^{-3}	2.82×10^{-3}
du/dy (1/s)	-1.41×10^{-5}	80.9	61.0	53.9	-7.24×10^{-7}	94.0	61.6	59.3
h (W/m ² K)	3.48	41.3	3.76	5.05	3.49	42.3	3.75	5.27
	1,464,575 elements				2,618,046 elements			
	A	B	C	D	A	B	C	D
$P(\text{N/m}^2)$	0.0234	0.0207	9.81×10^{-3}	-1.59×10^{-3}	0.0234	0.0207	9.81×10^{-3}	-1.59×10^{-3}
$\tau(\text{N/m}^2)$	1.26×10^{-10}	0.0110	1.14×10^{-3}	3.46×10^{-3}	1.26×10^{-10}	0.011	1.14×10^{-3}	3.46×10^{-3}
du/dy (1/s)	1.39×10^{-6}	119	62.0	68.1	1.39×10^{-6}	119	62.0	68.1
h (W/m ² K)	3.51	50.6	3.74	6.45	3.51	50.6	3.74	6.45

3. Results and Discussion

In order to conduct the study, some physical, hydrodynamic and thermal data are gathered from the recent publications [1,2–5,8–10,12]. The computational studies on the energy and exergy characteristics of the square cylinder (SC) are carried out at the Reynolds number range of $Re_B = 10$ – 50 , with the inlet air centerline-velocity range and the square cylinder edge value of $U_c = 4.319 \times 10^{-3}$ – 21.595×10^{-3} m/s and $B = 0.04$ m, respectively. Additionally, inlet air temperature, SC surface temperature and blockage ratio are chosen as $T_\infty = 333$ K, $T_s = 293$ K and $\beta = 0.800$ respectively. Energy characteristics are discussed under two sub-headings: *Momentum Characteristics* and *Thermal Characteristics*. Streamlines, temperature contours, velocity and temperature profiles, temperature gradients and mean temperature variations are discussed to describe the upstream, throat and downstream energy mechanisms. Exergy characteristics are presented with entropy generation values, by cross-correlating with mass flow rate, velocity and temperature variations, Reynolds number and with Bejan number, by demonstrating both the streamwise and spanwise variation styles.

Regardless of the scientific objectives of research studies, involving fluid flow and heat transfer mechanisms [1,4,7,10,11,42], the primary issue in the flowchart of the analysis is the evaluation of the hydrodynamic and thermal fields. Since the momentum and thermal characteristics constitute the fundamental information for the energy or exergy features of the laminar steady flow across the SC under strong blockage, the flow patterns and the thermal interactions around the SC become the essential outputs of the performed computations. Figure 2 displays the streamline formation (Figure 2a,c,e) and temperature contours (Figure 2b,d,f) in the flow field, bounded by the SC surfaces and the channel walls, for the Reynolds numbers of $Re = 10$ (Figure 2a,b), $Re = 30$ (Figure 2c,d) and $Re = 50$ (Figure 2e,f). The following discussions on the momentum, thermal and entropy generation characteristics of the upstream, throat and downstream domains of the SC will be carried out in conjunction with the information presented in Figure 2.

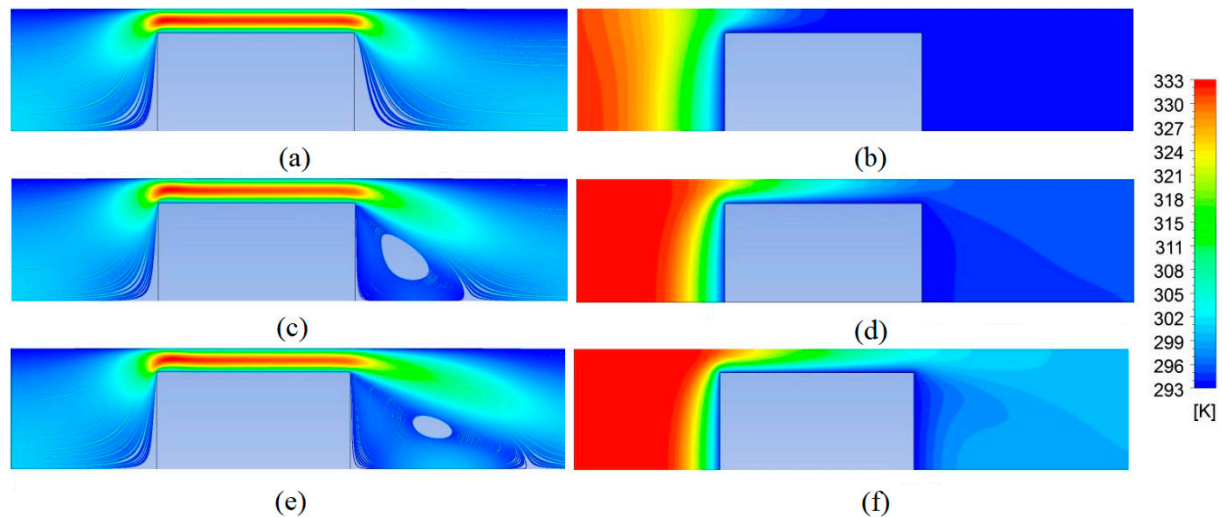


Figure 2. Streamline formation ((a), (c), (e)) and temperature contours ((b), (d), (f)) around the SC for the Reynolds numbers of $Re = 10$ ((a), (b)), $Re = 30$ ((c), (d)) and $Re = 50$ ((e), (f)).

3.1. Analysis in the Upstream Domain

3.1.1. Momentum Characteristics

Figure 3a shows the streamwise (u/U_o) and spanwise (v/U_o) non-dimensional velocity profiles in the upstream region of $x_{us} = 0-10$ mm for the Reynolds number range of $Re = 10-50$. It can be inspected from the figure that the hydrodynamic field senses the blockage action of the SC at $x_{us} = 10$ mm; such that the non-dimensional streamwise velocity values at the centerline deviate from $u/U_o = 1.5$ to $u/U_o = 0.635 \rightarrow 0.750$ ($Re = 10 \rightarrow 50$) and those of the spanwise values at $y = 0.015$ m deviate from zero to $v/U_o = 0.0028 \rightarrow 0.0124$ m/s. The order of the streamwise velocity profiles for different Reynolds numbers at $x_{us} = 10$ mm display two reverse locations at $y_{rl} \cong 0.013$ & 0.021 mm, where the zoomed plots provide a further detailed view. The physical background of this output can be clarified by the continuity phenomena (Equation (1)), such that the y_{rl} locations are close to the points where the u/U_o and v/U_o variations attain the highest values, respectively.

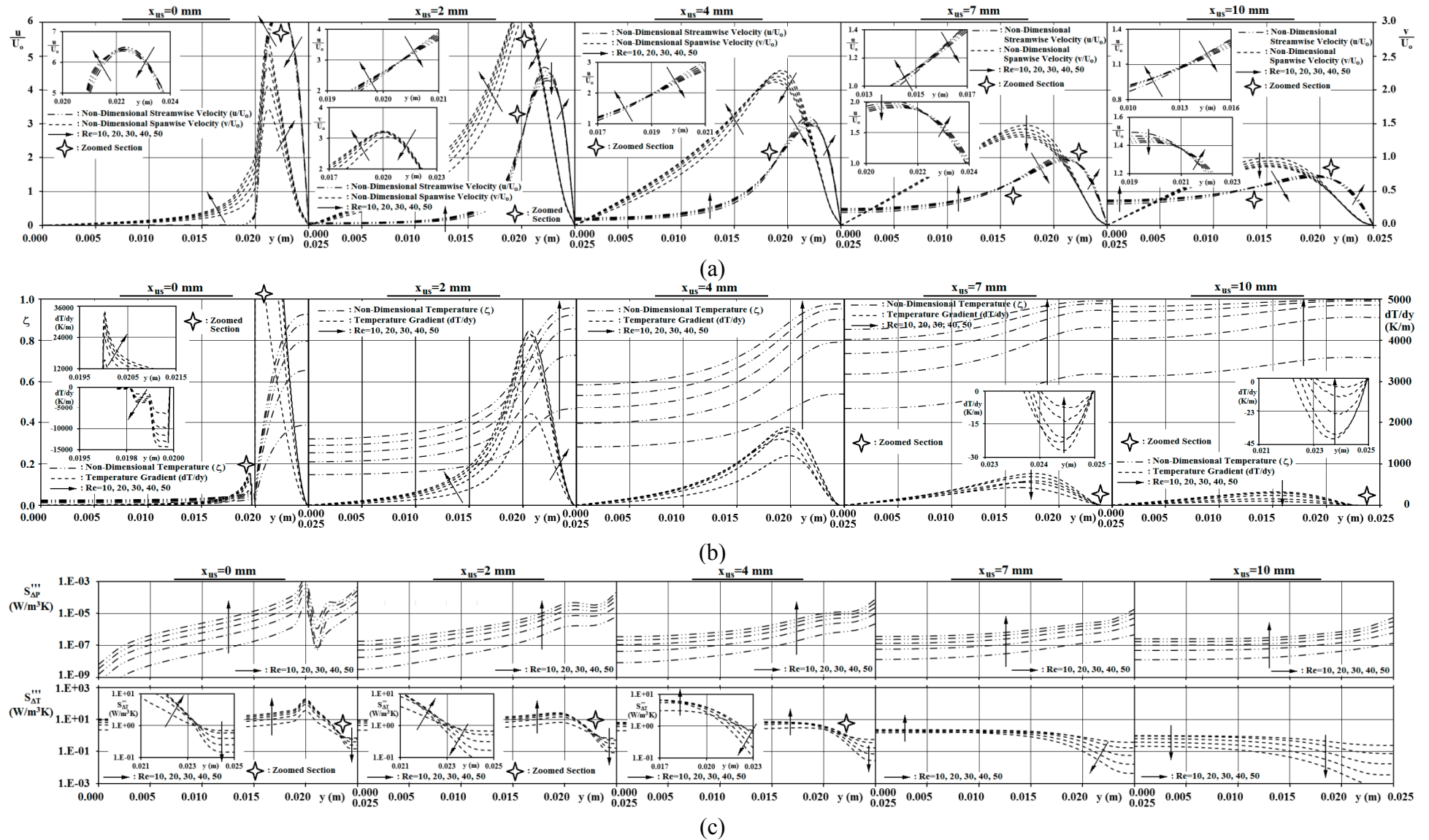


Figure 3. Upstream non-dimensional (a) velocity profiles, (b) temperature profiles and (c) local frictional and thermal entropy generation rates.

It can further be inspected from Figure 3a that, as the flow approaches the SC, stronger accelerations come into sight both in the streamwise and spanwise directions. This evaluation can be supported through the computed momentum parameters. Such that the accelerated flow results in the maximum non-dimensional velocity values of $(u/U_o)_{\text{Max}} = 2.025 \rightarrow 1.906$ and $(v/U_o)_{\text{Max}} = 1.475 \rightarrow 1.309$ at $x_{\text{us}} = 7$ mm; the corresponding data are $(u/U_o)_{\text{Max}} = 3.203 \rightarrow 2.941$, $4.658 \rightarrow 4.229$, $6.329 \rightarrow 6.330$ and $(v/U_o)_{\text{Max}} = 2.273 \rightarrow 2.115$, $3.036 \rightarrow 3.199$, $1.674 \rightarrow 2.700$ at $x_{\text{us}} = 4, 2, 0$ mm, respectively. The computed momentum parameters and the velocity profiles of Figure 3a simultaneously not only identify that as the flow approaches the SC ($x_{\text{us}} \rightarrow 0$ mm) the $(u/U_o)_{\text{Max}}$ and $(v/U_o)_{\text{Max}}$ data increase but also notify the grow of $(u/U_o)_{\text{Mean}}$ and $(v/U_o)_{\text{Mean}}$ data with higher Re for $x_{\text{us}} \leq 4$ mm. The analysis additionally showed that, in the streamwise direction ($x_{\text{us}} = 10 \rightarrow 0$ mm) the spanwise locations of the maximum values shift towards the inlet plane ($y = 0.020\text{--}0.025$ m) of the throat. This evaluation can be directly attributed to the regulation of the upstream streamlines of Figures 2a, 2c and 2e. The plots of $x_{\text{us}} = 0$ mm indicate that, regardless of the level of Reynolds number, the streamwise velocity values expand by an order of ≈ 6.35 ; however, those of the spanwise turn out to be dependent on Reynolds number with the $(v/U_o)_{\text{Max}}$ values of $1.67 \rightarrow 2.70$ (Re = $10 \rightarrow 50$). Besides, the mean values of u/U_o and v/U_o come out to be $u/U_o = 0.840 \rightarrow 0.879$ and $v/U_o = 0.236 \rightarrow 0.386$ at $x_{\text{us}} = 0$ mm, implying the stronger role of Reynolds number and blockage in the spanwise momentum activity. The close scientific link among the momentum characteristics and frictional entropy generation data ($S''''_{\Delta P}$) implies the significance of the discussions on the impacts of Reynolds number and local gradients.

3.1.2. Thermal Characteristics

The non-dimensional temperature distribution (ζ —Equation 16d) and the spanwise temperature gradients (dT/dy) in the upstream domain ($x_{\text{us}} = 0\text{--}10$ mm) of the SC are shown in Figure 3b. It can be seen from the figure that the cooling action of the SC is sensible around $x_{\text{us}} = 10$ mm, where the fluid domain appears to be most particularly influenced in the centerline ($y = 0$ mm) neighborhood with the lowest values of $\zeta = 0.625 \rightarrow 0.964$ (Re = $10 \rightarrow 50$). Although the presence of the SC is thermally noticeable in the highest Reynolds number case of Re = 50 even at $x_{\text{us}} = 10$ mm, computations put forward slight temperature drop in the flow domain through the ζ_{Mean} and ζ_{Max} values of 0.980 and 0.997 respectively. On the other hand the corresponding data are computed as $\zeta_{\text{Mean}} = 0.670$ and $\zeta_{\text{Max}} = 0.719$ in the flow scenario with Re = 10. The comparably lower ζ values due to weaker momentum activity can be attributed to the accompanied less mass flow rates. The figure also puts forward that, flows with lower mass flow rate, thus low Reynolds number, are more sensible to heat transfer and temperature drop in the earlier section ($x_{\text{us}} > 7$ mm) of the upstream region. For the particular issue at $x_{\text{us}} = 7$ mm, numerical analysis identifies that, as the mean and maximum non-dimensional temperature values of the Re = 50 case become $\zeta_{\text{Mean}} = 0.915$ and $\zeta_{\text{Max}} = 0.991$, the corresponding values of the Re = 10 scenario appears as $\zeta_{\text{Mean}} = 0.538$ and $\zeta_{\text{Max}} = 0.638$. This finding can as well be associated with thicker thermal boundary layers and weaker heat transfer activity in low Reynolds numbers.

In the closer flow domains of the SC ($x_{\text{us}} \leq 4$ mm), the thermal texture of the higher Reynolds number scenarios are found to be more motivated. Computations showed that as the non-dimensional centerline temperature value drops from $\zeta = 0.585$ ($x_{\text{us}} = 4$ mm) to $\zeta = 0.025$ ($x_{\text{us}} = 0$ mm) at Re = 50, those of the Re = 10 case are $\zeta = 0.281$ and $\zeta = 0.012$. The intense streamwise temperature drop

mechanism in higher Reynolds numbers, neighboring the front-surface, is not only reliable evidence of thinner thermal boundary layer and higher heat transfer rates, but can also be considered as scientific projection for encouraged thermal entropy generation. On the other hand, the temperature values of the projecting trajectory to the throat ($y = 0.020\text{--}0.025$ m) are regularly above those of the line of action of the SC (LASC—Figure 1a). This outcome is mostly due to the adiabatic stand of the channel walls. As the temperature drop of the flow scenario with the highest inlet velocity case ($Re = 50$) at the duct wall ($y = 0.025$ m) is insensible with the values of $\zeta = 0.997\text{--}0.926$ ($x_{us} = 10\text{--}0$ mm), those of the lowest inlet velocity flow ($Re = 10$) put forward the inverse trends in thermal actions and mass flow rates with the values of $\zeta = 0.719\text{--}0.387$. The comparably higher heat capacity of the flows in higher Reynolds numbers as well indicates the correlatively remained additional energy for exergy destruction in the throat.

Figure 3b further displays the spanwise temperature gradients (dT/dy) in the upstream region. The findings on dT/dy are scientifically important due to their direct contribution to thermal entropy generation through Equation (6). The expanding character of the dT/dy values in the streamwise direction ($x_{us} = 10\text{--}0$ mm) for all Reynolds numbers indicate the growing thermal activity. Augmentation of heat transfer rates with Reynolds number, in the mild blockage case of $\beta = 1/8$, was also documented by Rahnama and Hadi [13]. Computations enlighten this determination through the mean and maximum values of the spanwise temperature gradients of $(dT/dy)_{Mean} = 146.9\text{--}52.6$ K/m and $(dT/dy)_{Max} = 296.4\text{--}97.6$ K/m ($Re = 10\text{--}50$) at $x_{us} = 10$ mm and $(dT/dy)_{Mean} = 600.7\text{--}1441$ K/m and $(dT/dy)_{Max} = 15415.8\text{--}34102.2$ K/m at $x_{us} = 0$ mm. The higher temperature gradients in the closer sections to the SC indicate the presence of enhanced thermal entropy generation rates in the corresponding regions. Besides, the paramount dT/dy values appear around $y = 0.020$ m, especially for $x_{us} \leq 4$ mm, which can be explained by the thermal mixing of the comparably cooler flow in the line of action of the SC ($y = 0\text{--}0.020$ m) than those of the throat's projecting trajectory. The thermal interactions generate secondary temperature gradients in the spanwise direction, where the most recognizable sections, especially at $x_{us} = 0$ mm, are displayed in zoomed style in Figure 3b. The figure provides additional information on the thermal characteristics of the projecting trajectory of the throat (PTT—Figure 1a) through the dT/dy results. Due to the distance with the SC, the flow in the vicinity of the duct wall exhibits late and weak thermal response. As a consequence of this phenomenon, Figure 3b, in terms of ζ , and Figure 2b,d,f, in terms of temperature contours, display sub-hot domains in the neighborhoods of the duct wall. As a result, the upstream domain, especially for $x_{us} \leq 7$ mm, experiences temperature deviations, becoming more significant on the front-surface ($x_{us} = 0$ mm).

3.1.3. Entropy Generation Characteristics

Variation of local frictional ($S''_{\Delta P}$) and thermal ($S''_{\Delta T}$) entropy generation rates, for the considered Reynolds number range in the upstream domain of the SC, are shown in Figure 3c. Since the $S''_{\Delta P}$ data mainly depend on the streamwise and spanwise velocity gradients, the momentum mechanisms of the flow domain (Figure 3a) constitute the scientific background. At the upstream location of $x_{us} = 10$ mm, the $S''_{\Delta P}$ distributions show almost linear trends and resemble comparable augmentation rates in the spanwise direction (y); besides the $(S''_{\Delta P})_{Max}/(S''_{\Delta P})_{Mean}$ ratio attains the values of $4.087\text{--}7.259$ for $Re = 10\text{--}50$ indicating the impact of Reynolds number or flow velocity on the frictional entropy

generation rates. On the other hand, as the flow approaches the SC the duct wall entropy generation values show higher augmentation rates when compared to those of the centerline, where the identical ratio grows up to 13.153→13.084 at $x_{us} = 0$ mm. It can further be inspected from the figure that, as the flow approaches to the SC ($x_{us} = 10 \rightarrow 0$ mm), the $S'''_{\Delta P}$ values of the duct wall ($y = 25$ mm) grow continuously. The tabulated mean and maximum values of $S'''_{\Delta P}$ in Table 2 display the matching information, where this finding has close link with the duct wall velocity gradients and can as well be connected with the frictional activity. In fact, considerably rapid augmentations in $S'''_{\Delta P}$ are observed for $x_{us} \leq 2$ mm, where the flow firmly orients to enter the throat, causing the streamlines to squeeze and become denser locally (Figure 2a,c,e). The most remarkable $S'''_{\Delta P}$ values are attained at the inlet section ($x_{us} = 0$ mm) of the throat, specifically on the corner of the SC ($y = 20$ mm). This finding can be explained by not only the presence of the unguided mixing but also the maximum accelerations recorded throughout the domain (Figure 3a and Table 2).

Table 2. Upstream entropy generation parameters for various x_{us} sections and Re cases.

	x_{us} (mm)	Re = 10	Re = 20	Re = 30	Re = 40	Re = 50
$(S'''_{\Delta P})_{Mean}$ (W/m ³ K)	0	1.957×10^{-6}	9.111×10^{-6}	2.324×10^{-5}	4.589×10^{-5}	7.872×10^{-5}
		2.574×10^{-5}	1.18×10^{-4}	3.00×10^{-4}	5.95×10^{-4}	1.03×10^{-3}
	2	7.139×10^{-7}	2.655×10^{-6}	6.762×10^{-6}	1.217×10^{-5}	1.93×10^{-5}
		6.567×10^{-6}	2.804×10^{-5}	6.782×10^{-5}	0.0001	0.0002
	4	2.908×10^{-7}	1.13×10^{-6}	2.52×10^{-6}	4.51×10^{-6}	7.16×10^{-6}
$(S'''_{\Delta P})_{Max}$ (W/m ³ K)	4	2.273×10^{-6}	9.678×10^{-6}	2.38×10^{-5}	4.65×10^{-5}	7.98×10^{-5}
		7	8.528×10^{-8}	3.281×10^{-7}	7.32×10^{-7}	1.31×10^{-6}
	7	4.713×10^{-7}	2.079×10^{-6}	5.281×10^{-6}	1.06×10^{-5}	1.84×10^{-5}
		10	3.242×10^{-8}	1.233×10^{-7}	2.72×10^{-7}	4.82×10^{-7}
	1.325×10^{-7}	6.036×10^{-7}	1.56×10^{-6}	3.15×10^{-6}	5.502×10^{-6}	
$(S'''_{\Delta T})_{Mean}$ (W/m ³ K)	0	4.515	10.162	14.719	18.689	22.364
		36.607	91.509	132.00	164.00	193.00
	2	2.912	5.891	8.195	10.087	11.714
		6.474	14.086	19.451	23.338	26.208
	4	2.100	3.680	4.560	5.070	5.360
$(S'''_{\Delta T})_{Max}$ (W/m ³ K)	4	3.080	5.452	6.476	6.993	7.306
		7	1.254	1.603	1.505	1.277
	7	1.571	2.222	2.331	2.165	1.877
		10	0.689	0.555	0.335	0.184
	0.974	0.933	0.638	0.384	0.215	
Be_{Mean} Be_{Max}	0	0.999	0.999	0.999	0.999	0.999
		1.000	1.000	1.000	0.999	1.000
	2	0.999	0.999	0.999	0.999	0.999
		0.999	0.999	0.999	0.999	0.999
	4	0.999	1.000	0.999	0.999	0.999
		0.999	1.000	0.999	0.999	0.999
	7	0.999	0.999	0.999	0.999	0.999
		0.999	0.999	0.999	0.999	0.999
	10	0.999	0.999	0.999	0.999	0.999
		0.999	0.999	0.999	0.999	0.999

The kinky structure in $S_{\Delta P}'''$ distributions becomes identifiable at $x_{us} = 4$ mm. Indeed, this pattern can be explained by the nearing of the maximum locations of the streamwise (u) and spanwise (v) velocity profiles (Figure 3a). As the spanwise positions of the maximum values of the u and v components shift in the streamwise domain of $x_{us} = 4 \rightarrow 0$ mm (Figure 3a), the second kink representing the local comes into sight at $x_{us} = 0$ mm. It can be verified that as the kink, pointing out the maximum $S_{\Delta P}'''$ ($x_{us} = 4 \rightarrow 0$ mm), is close to the peak position of the u/U_o profile, that of the minimum $S_{\Delta P}'''$ ($x_{us} = 0$ mm) is positioned in between the peak locations of u/U_o and v/U_o . Similar to the impact of Reynolds number on momentum characteristics, frictional entropy generation values are computed to grow with Reynolds number as well. Table 2 further indicates the expanding attitude of $S_{\Delta P}'''$ with Reynolds number. Computations showed that as the ratio of the mean frictional entropy generation values of the flows with $Re = 50$ and $Re = 10$ is $(S_{\Delta P}''')_{\text{Mean-}Re=50}/(S_{\Delta P}''')_{\text{Mean-}Re=10} = 23.38$ at $x_{us} = 10$ mm, it grows up to 40.22 at $x_{us} = 0$ mm clarifying the rapid augmentations for $x_{us} \leq 2$ mm. On the other hand, the ratio of the $(S_{\Delta P}''')_{\text{Max}}$ values come out to be in the narrow band of 40.15–41.52 for the complete upstream domain ($x_{us} = 10 \rightarrow 0$ mm) specifying similar variations with Re in the momentum mechanisms on the duct wall. Additionally, towards the SC ($x_{us} = 10 \rightarrow 0$ mm) the centerline ($y = 0$ mm) $S_{\Delta P}'''$ values continuously decrease, where the drops become remarkable for $x_{us} < 2$ mm. This outcome can be associated with the deceleration of the streamwise velocity values at the centerline, which results with the completely stagnant flow on the front-surface of the SC ($x_{us} = 0$ mm & $y = 0$ mm).

The thermal part ($S_{\Delta T}'''$) of entropy generation displays two different characteristics in the upstream and downstream sections of $x_{us} = 7$ mm. As described in Figure 3b, when compared with low Reynolds number cases, the flows with higher Reynolds numbers respond to the presence of the SC in the further sections of the streamwise direction. This behavior delays the thermal interactions of the fluid flow with the solid SC up to the neighborhoods of the front-surface. The so structured thermal layouts (Figure 2b,d,f) exhibit comparably higher temperature gradients in lower Reynolds number flows for $x_{us} \geq 7$ mm (Figure 3b); thus, the $S_{\Delta T}'''$ data of the high Re flows come up to be lower. Table 2 outlines this output with the mean thermal entropy generation values of $(S_{\Delta T}''')_{\text{Mean}} = 0.095 \rightarrow 0.689$ W/m³K ($Re = 50 \rightarrow 10$). However, in closer sections to the SC ($x_{us} \leq 4$ mm) the flows with high Re interact with the SC developing thinner thermal boundary layers and greater temperature gradients, which promotes the thermal entropy generation values as well. In particular, on the front-surface of the SC ($x_{us} = 0$ mm), computations revealed the $(S_{\Delta T}''')_{\text{Mean}}$ values of 22.364 W/m³K and 4.515 W/m³K for flows with $Re = 50$ and $Re = 10$, respectively (Table 2). It must additionally be recognized from the figure that, even at high Reynolds numbers the flow on the duct walls ($y = 25$ mm) is persistent to sustain its thermal capacity, resulting in lower $S_{\Delta T}'''$ values. The zoomed plots of $x_{us} \leq 4$ mm identify the mechanism by indicating sub thermal-regions at $y > 0.023$ m. The temperature contours in Figure 2d,f show the uninfluenced stand of the thermal composition on the duct wall, even up to the inlet plane of the throat. On the other hand, similar to the findings on $S_{\Delta P}'''$, the most remarkable ascents in $S_{\Delta T}'''$ are also located around the inlet corner of the SC ($x_{us} = 0$ mm and $y = 20$ mm). Table 2 further displays information on the variation of Bejan number (Equation (8)) with upstream section and Reynolds number. The unchangingly constant value of $Be = 1$ remarks that, almost the entire exergy destruction mechanism in low Reynolds number ($Re \leq 50$) channel flows is in terms of thermal entropy

3.2. Analysis in the Throat Domain

3.2.1. Momentum Characteristics

Figure 4a displays the streamwise and spanwise velocity profiles for the Reynolds number range of $Re = 10\text{--}50$, throughout the complete throat length of $x_{th} = 0\text{--}40$ mm. The extremely bended streamlines (Figure 2a,c,e) at the inlet section ($x_{th} = 0$ mm) of the throat can as well be visualized in Figure 4a; the performed computations point out that the augmented spanwise velocity values grow up to $v/U_o = 1.670\text{--}2.700$ ($Re = 10\text{--}50$). The maximum values are mostly located around $y = 0.021$ m, being close to the solid top surface of the SC. The irregular form of v/U_o profiles at $x_{th} = 0$ mm strictly outlines the distress in the flow, which is accompanied by strong velocity gradients and undeveloped behavior both in the downstream ($x_{th} < 0$ mm) and upstream ($x_{th} > 0$ mm) domains. Thus, the profiles at $x_{th} = 0$ mm can be considered to be responsible for exergy destruction in the corresponding zone. Being in conjunction with the spanwise velocity values, those of the streamwise as well demonstrate an asymmetric distribution. The major portion of the flow rate seems to be squeezed in the neighborhood of the SC, where the mean values of streamwise velocity are computed as $u/U_o = 3.637\text{--}3.795$ ($Re = 10\text{--}50$). However, in the streamwise direction the flow becomes fully developed rapidly ($x_{th} = 10$ mm) due to the strict guidance of the throat; such that the spanwise motion vanishes ($v = 0$).

The streamwise velocity values accelerate up to $u/U_o = 6.381\text{--}6.789$ ($Re = 10\text{--}50$), where the maximum values are located exactly at the symmetry axis ($y = 0.0225$ m) of the throat, verifying the fully developed character. On the other hand, the slight gap of 0.408 among those of $Re = 10$ and $Re = 50$ rely on the enhanced cooling rate of the flow in the $Re = 10$ case, when compared to those of the higher Reynolds number cases (Figure 2b,d,f). The inverse relation of temperature and density (Equation (15d)) has further role on the velocity values through the mass flow rate issue (Equation (16c)) of the momentum mechanism. Indeed, as the flow proceeds downstream ($x_{th} > 10$ mm) additional cooling results in marked decreases in the u data, where the maximum values become $u/U_o = 6.317\text{--}6.546$ at $x_{th} = 30$ mm in line with expectations based on fundamental fluid mechanics principles. At the exit zone of the throat ($x_{th} \approx 40$ mm) the flow domain is intensely disturbed resulting in the emerging of spanwise velocities and deviations in the streamwise velocity profiles. Computations revealed that, the mean streamwise velocity data at $x_{th} = 40$ mm come out to be lower than those of the inlet plane ($x_{th} = 0$ mm) results, with the particular values of $u/U_o = 3.509\text{--}3.617$. This outcome can be associated with the above denoted statement on the interaction of temperature, density and velocity. As the jets are persistently oriented towards the symmetry axis of the duct (Figure 2a,c,e), the most comprehensive values appear close to the top-surface ($y = 0.020$ m) of the SC. However, computational evaluations put forward that the maximum values of the spanwise velocity at the throat exit ($x_{th} = 40$ mm) come out to be $v/U_o = -1.090\text{--}-0.551$ ($Re = 10\text{--}50$), which are, in absolute value approach, lower than those of the inlet plane ($x_{th} = 0$ mm), which can be regarded as a sign of stronger frictional activity downstream of $x_{th} = 40$ mm on the duct wall than the amount of friction upstream of $x_{th} = 0$ mm.

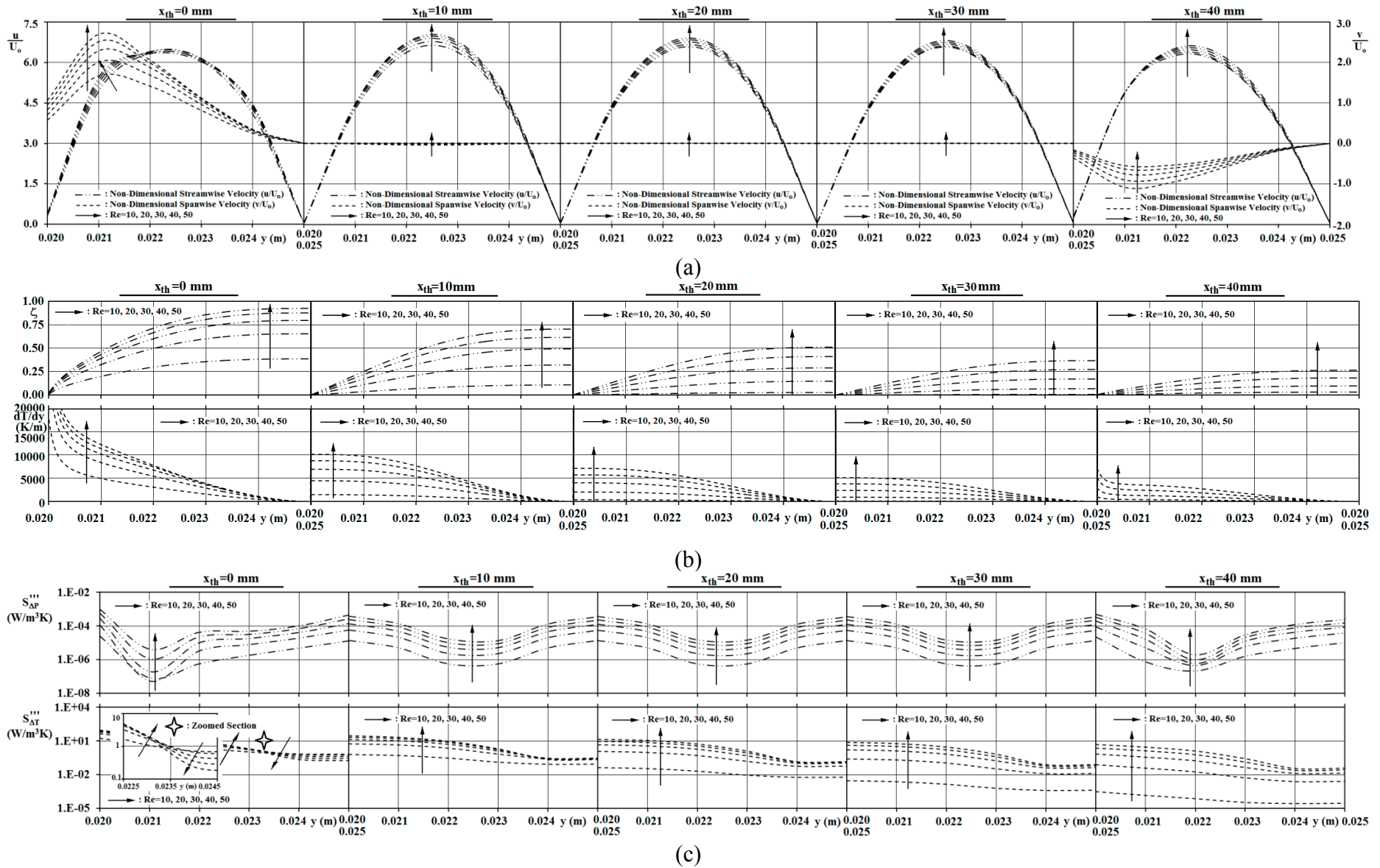


Figure 4. Throat non-dimensional (a) velocity profiles, (b) temperature profiles and (c) local frictional and thermal entropy generation rates.

3.2.2. Thermal Characteristics

Figure 4b displays the non-dimensional temperature (ζ) and spanwise temperature gradient (dT/dy) variations in the throat for different Reynolds number cases. It can be seen from Figure 4b that, due to the advanced cooled state of the lower Re cases, their flow temperature values are poorer throughout the throat. The computed thermal parameters detail the additional cooling action in the throat with particular data, where the duct wall ($y = 0.025$ m) temperature drops from $\zeta = 0.387 \rightarrow 0.926$ ($Re = 10 \rightarrow 50$) at $x_{th} = 0$ mm to $\zeta = 0.002 \rightarrow 0.266$ at $x_{th} = 40$ mm. Detailed inspection points out that, at the lowest Reynolds number case of $Re = 10$ the mean fluid temperature drops almost down to the surface temperature of the SC ($T = 293$ K— $\zeta_{Mean} = 0.018$) even at $x_{th} = 20$ mm; the corresponding state ($\zeta_{Mean} = 0.021$) for the $Re = 20$ scenario is observed at $x_{th} = 40$ mm. These findings are completely in harmony with the temperature contours of Figure 2b,d,f; moreover, the decay of temperature values will as well result in the steep decline of exergy destruction in terms of $S_{\Delta T}'''$. On the other hand, the hotter fluid domains in the inlet section ($x_{th} = 0$ mm) of the throat, attained at higher Re cases, stand for comparably advanced thermal activity. Dhiman *et al.* [43] also reported the streamwise decay of heat transfer rates on the top-surface of the SC under the weak blockage of $\beta = 1/20$. These mechanisms are accompanied by the stronger temperature gradients of $(dT/dy)_{Mean} = 7239.9 \rightarrow 3022.9$ K/m ($Re = 50 \rightarrow 10$); the superior thermal task in flows with high Re can be associated with higher $S_{\Delta T}'''$ through Equation (6) in the corresponding regions.

3.2.3. Entropy Generation Characteristics

Frictional ($S_{\Delta P}'''$) and thermal ($S_{\Delta T}'''$) entropy generation values throughout the throat ($x_{th} = 0 \rightarrow 40$ mm) above the top-surface of the SC for various Reynolds numbers are plotted in Figure 4c. It can be inspected from the figure that the dependence of $S_{\Delta P}'''$ and $S_{\Delta T}'''$ characteristics on Reynolds number comply completely with those of the momentum and thermal characteristics, where both components of entropy generation grow with Reynolds number. Further identifying the concurrent behaviors of momentum characteristics and frictional entropy generation data, the lowest $S_{\Delta P}'''$ are located exactly at the midplane of the throat ($y = 0.025$ m), where the local maxima of the u/U_o profiles are evaluated in the throat domain of $x_{th} = 10\text{--}30$ mm. Moreover, either of the $S_{\Delta P}'''$ and $S_{\Delta T}'''$ distributions of the inlet section ($x_{th} = 0$ mm) imply significant disturbances which can entirely be attributed to the second-order behaviors in the momentum (Figure 4a) and thermal (Figure 4b) mechanisms at the identical zone. The particular issue in the $S_{\Delta T}'''$ distributions is the reverse order around $y \cong 0.023$ m, which can be explained by the almost unaffected temperature values ($\zeta \approx 1$) at high Re cases (Figure 4b) in the neighborhood of the duct wall ($y > 0.023$ m). Thus, it can further be detailed that, in the inlet domain of the throat ($x_{th} = 0\text{--}10$ mm) the flow in the vicinity of the duct wall ($y = 0.025$ m) experiences stronger streamwise variations (dT/dx) than that of the spanwise (dT/dy). This thermal pattern results in the developing $S_{\Delta T}'''$ layout in the neighborhood of the duct wall ($y > 0.023$ m) in the corresponding streamwise zone ($x_{th} = 0\text{--}10$ mm).

It can also be inspected from the temperature contours of Figure 2f that, flow enters the throat with almost $T \cong 333$ K in the indicated particular sub-domain. Besides, the throat physically constrains the flow and disciplines both of the momentum and thermal activities; such that a 10 mm flow distance was sufficient to generate fully developed velocity (Figure 4a) and temperature (Figure 4b) profiles. As a consequence, $S_{\Delta P}'''$ profiles attain symmetric forms depending only on the streamwise velocity distributions (u/U_o) due to the expiry of the spanwise values (v/U_o —Figure 4a). Indeed, this mechanism

in $S'''_{\Delta P}$ lasts up to the exit section of the throat.

Table 3. Throat entropy generation parameters for various x_{th} sections and Re cases.

	x_{th} (mm)	Re = 10	Re = 20	Re = 30	Re = 40	Re = 50
$(S'''_{\Delta P})_{Mean}$ (W/m ³ K) $(S'''_{\Delta P})_{Max}$ (W/m ³ K)	0	7.77×10^{-6}	3.48×10^{-5}	8.61×10^{-5}	1.66×10^{-4}	2.82×10^{-4}
		2.57×10^{-5}	1.18×10^{-4}	3.00×10^{-4}	5.95×10^{-4}	1.03×10^{-3}
	10	6.62×10^{-6}	2.71×10^{-5}	6.22×10^{-5}	1.12×10^{-4}	1.76×10^{-4}
		1.43×10^{-5}	5.95×10^{-5}	1.3×10^{-4}	2.50×10^{-4}	3.93×10^{-4}
	20	6.56×10^{-6}	2.66×10^{-5}	6.09×10^{-5}	1.09×10^{-4}	1.73×10^{-4}
		1.41×10^{-5}	5.74×10^{-5}	1.32×10^{-4}	2.39×10^{-4}	3.81×10^{-4}
	30	6.55×10^{-6}	2.64×10^{-5}	6.01×10^{-5}	1.08×10^{-4}	1.70×10^{-4}
		1.40×10^{-5}	5.66×10^{-5}	1.29×10^{-4}	2.35×10^{-4}	3.72×10^{-4}
	40	6.81×10^{-6}	2.71×10^{-5}	6.05×10^{-5}	1.06×10^{-4}	1.64×10^{-4}
		2.30×10^{-5}	9.26×10^{-5}	2×10^{-4}	3.41×10^{-4}	5.09×10^{-4}
$(S'''_{\Delta T})_{Mean}$ (W/m ³ K) $(S'''_{\Delta T})_{Max}$ (W/m ³ K)	0	4.804	11.99	17.02	20.59	23.36
		17.80	47.40	68.20	83.50	96.40
	10	0.303	2.384	5.432	8.366	10.880
		0.656	5.959	14.358	22.904	30.573
	20	0.021	0.509	1.889	3.734	5.693
		0.044	1.246	4.849	9.816	15.213
	30	0.001	0.109	0.674	1.667	2.975
		0.003	0.264	1.715	4.328	7.841
	40	0.0001	0.025	0.225	0.778	1.617
		0.0003	0.080	0.714	2.458	5.043
Be_{Mean} Be_{Max}	0	0.999	0.999	0.999	0.999	0.999
		1.000	1.000	0.999	1.000	1.000
	10	0.999	0.999	0.999	0.999	0.999
		0.999	0.999	0.999	0.999	0.999
	20	0.999	0.999	0.999	0.999	0.999
		0.999	0.999	0.999	0.999	0.999
	30	0.991	0.999	0.999	0.999	0.999
		0.999	0.999	0.999	0.999	0.999
	40	0.911	0.996	0.998	0.998	0.998
		0.997	0.999	0.999	0.999	0.999

In addition to the augmentation of frictional entropy generation values with Reynolds number, Table 3 further shows that as the ratio of the mean frictional entropy generation values of the flows with $Re = 50$ and $Re = 10$ is $(S'''_{\Delta P})_{Mean-Re = 50} / (S'''_{\Delta P})_{Mean-Re = 10} = 36.29$ at $x_{th} = 0$ mm, it drops down to 24.08 at $x_{th} = 40$ mm indicating that the impact of Re on $S'''_{\Delta P}$ decreases in the flow direction inside the throat. Besides, regardless of the level of Reynolds number, the frictional entropy generation data are evaluated to decrease in the streamwise direction. The $(S'''_{\Delta P})_{Mean-x_{th} = 40 \text{ mm}} / (S'''_{\Delta P})_{Mean-x_{th} = 0 \text{ mm}}$ ratio comes out to be 0.876→0.582 for $Re = 10 \rightarrow 50$, which can be attributed to the comparably lower deviations in the v/U_o profiles of Figure 4a at the throat exit ($x_{th} = 40$ mm) in the high Reynolds number case of $Re = 50$.

In the lowest Reynolds number ($Re = 10$) scenario, fast declines in $S'''_{\Delta T}$ are observed for $x_{th} \geq 10$ mm, which can be explained by the rapid cooling ($\zeta \rightarrow 0$) characteristics (Figure 4b). Table 3 identifies this output with the mean $S'''_{\Delta T}$ values of 4.804→0.0001 W/m³K for $x_{th} = 0 \rightarrow 40$ mm. Moreover, the core

temperature values ($\zeta \approx 1$) of even the highest Reynolds number case of $Re = 50$ turn out to be thermally incapable to penetrate inside the throat and access the section of $x_{th} = 10$ mm. Therefore, the order of the $S'''_{\Delta T}$ distributions becomes uniform for $x_{th} \geq 10$ mm (Figure 4c). Since the temperature profiles at the exit plane express no individual variation, the $S'''_{\Delta T}$ characteristics retain their routine layout at $x_{th} = 40$ mm as well. Thus, the thermal entropy generation data decrease in a demanding manner in the streamwise direction for the complete Reynolds number range (Table 3). However, the exit plane jets (Figures 2a,c,e, and 4a) triggers the onset of the spanwise fluid flow (v) and disturbs the fully developed form of the streamwise velocity profiles. As a consequence, the style and symmetry of the $S'''_{\Delta P}$ profiles also become corrupted at the exit plane. The impact of this distress results in sensible deviations on the Bejan number, especially at the lowest Reynolds number case of $Re = 10$, with the mean value of $Be_{Mean} = 0.911$ at $x_{th} = 40$ mm (Table 3).

3.3. Analysis in the Downstream Domain

3.3.1. Momentum Characteristics

The streamwise and spanwise velocity distributions in the downstream region of the SC are shown in Figure 5a. The exit plane ($x_{th} = 40$ mm) momentum characteristics of the throat displayed in Figure 4a coincide with the $x_{ds} = 0$ mm profiles of the $y = 0.020$ – 0.025 m zone in Figure 5a. Due to the no-slip condition on the back-surface of the SC, both of the streamwise and spanwise velocities attain the value of zero on the solid wall ($y = 0$ – 0.020 m) at $x_{ds} = 0$ mm. As the flow moves forward in the downstream domain, the motivation of the flow to separate by generating a vortex structure can even be seen at $x_{ds} = 2$ mm through the negative values of the streamwise velocity ($u/U_o < 0$). In addition, the strength of vortex development in the Reynolds case of $Re = 50$ is evident with the comparably advanced upward values of spanwise velocity, particularly in the $y = 0$ – 0.020 m region. Besides, as detailed in the zoomed plot of $x_{ds} = 2$ mm, the order of the streamwise velocity values for different Reynolds number scenarios become altered around $y \approx 0.020$ m. This evaluation can be attributed to the thermal mixing in the neighboring zone as shown in Figure 2b,d,f. This output can also be considered as a source of thermal entropy generation in the corresponding location. In the further downstream sections ($x_{ds} \geq 4$ mm) comparably enhanced reverse flows (negative streamwise velocities) are recorded in the lower part ($y = 0$ – 10 mm) of the vortex. However, the peak velocities appear to attain lower values; such that the computed momentum parameters particularly identify the $(u/U_o)_{Max}$ as $6.270 \rightarrow 6.540$ ($Re = 10 \rightarrow 50$) at $x_{ds} = 0$ mm and $1.822 \rightarrow 4.191$ at $x_{ds} = 10$ mm. These records as well correspond to lower velocity gradients and stand for reduced frictional entropy generation preferred by Breuer *et al.* [10], the structure and formation of the downstream vortex system can further be discussed through the spanwise velocity layout in the region of $x_{ds} = 0$ – 10 mm. The v/U_o variation in the y -direction at the lowest Reynolds number of $Re = 10$ shows no sign of counter-flow having regular negative values (Figure 5a). On the other hand, the positive v/U_o values of $Re \geq 20$ cases indicate the presence of the vortex, which interacts with the back-surface of the SC. The strength and occupied domain of the vortex have a close relation with the magnitude of the upward spanwise velocity values ($v/U_o > 0$) in the separated flow domain, next to back-surface ($y = 0$ – 20 mm, Figure 5a).

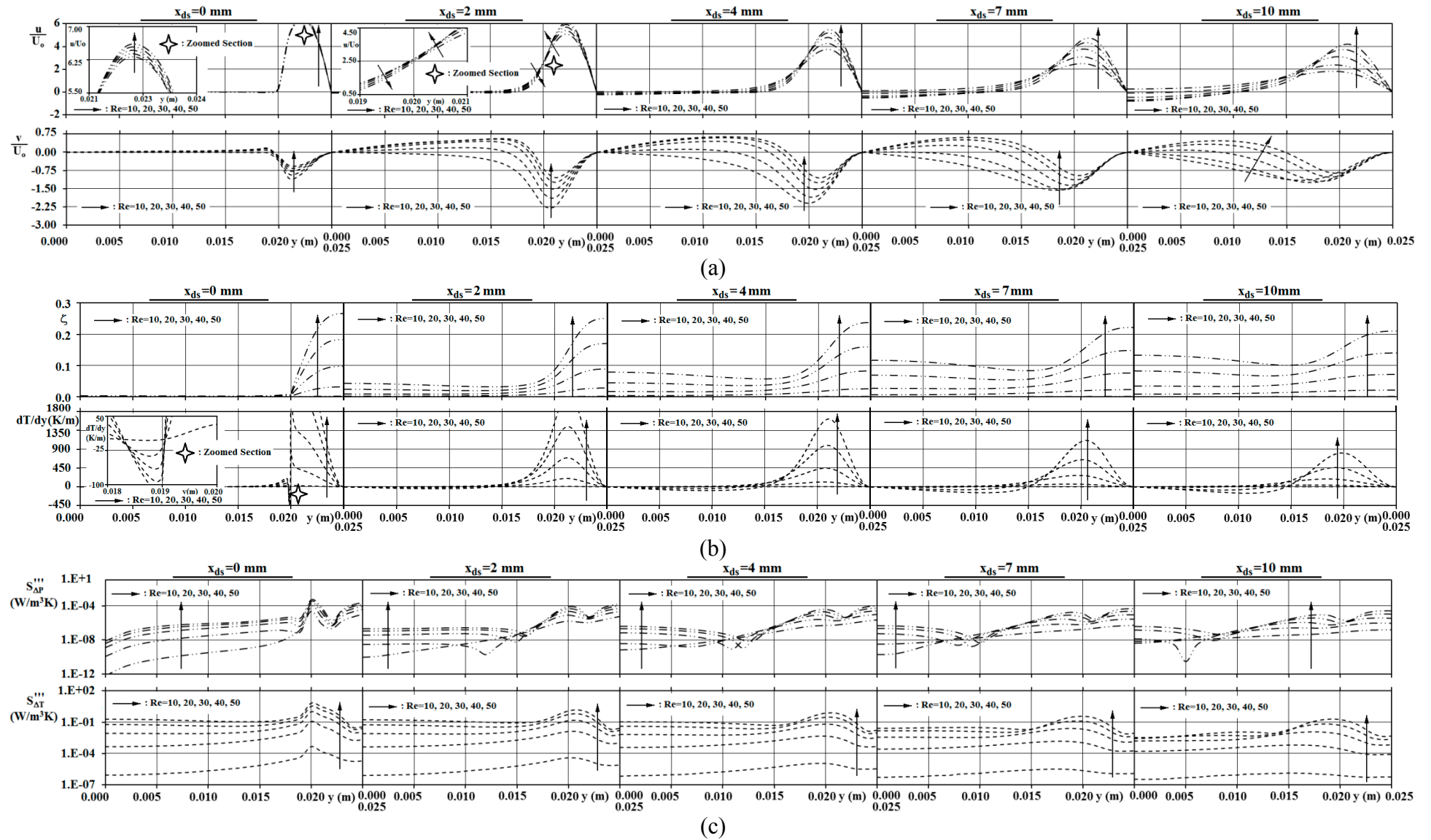


Figure 5. Downstream non-dimensional (a) velocity profiles, (b) temperature profiles and (c) local frictional and thermal entropy generation rates.

The above stated recognition puts forward the stronger vortex activity at higher Reynolds numbers, where this finding shows parallelism with the vortex scenes of Figure 2c,e. Breuer *et al.* [10] and Rahnama and Hadi [13] as well reported expanded recirculation zones with higher Reynolds numbers in the downstream region of a confined SC. Figure 5a and the momentum parameters identify that the spanwise velocities become weaker in the downstream direction; even the v/U_o data of the $Re = 20$ case transform to attain negative values at $x_{ds} = 7$ mm ($(v/U_o)_{Mean} = -0.482$, $(v/U_o)_{Max} = -1.540$), indicating the completion of the recirculation zone. Similar to the streamwise velocity distributions, the spanwise values as well show the most significant gradients in the exit path ($y = 0.020$ – 0.025 m) of the throat; but they become milder in the downstream direction ($x_{ds} = 0$ → 10 mm). These evaluations can be considered as reliable foresights for the frictional entropy generation values in the downstream region of the SC.

3.3.2. Thermal Characteristics

The non-dimensional temperatures (ζ) and the temperature gradient (dT/dy) values in the downstream region of the SC are plotted in Figure 5b. It must be indicated that the ζ profiles of $x_{ds} = 0$ mm correspond to those of the Figure 4b for $x_{th} = 40$ mm. It can be inspected from the figure that, the temperature values of the SC's line of action ($y = 0$ – 0.020 m) augment in the flow direction ($x_{ds} = 0$ → 10 mm); however the reverse mechanism is set for the projecting trajectory of the throat. The computed thermal parameters identify these evaluations in terms of mean and maximum temperature values, which refer mainly to the SC's line of action and the upper physical boundary ($y = 0.025$ m) of the projecting trajectory. As the line of action data is $\zeta_{Mean} = 0.000$ → 0.014 ($x_{ds} = 0$ → 10 mm) and $\zeta_{Mean} = 0.043$ → 0.137 for the $Re = 20$ and $Re = 50$ cases, respectively, those of the projecting trajectory are recorded as $\zeta_{Max} = 0.032$ → 0.022 ($Re = 20$) and $\zeta_{Max} = 0.266$ → 0.211 ($Re = 50$). Simultaneous evaluation of the two mechanisms clarifies the presence of thermal mixing, which mostly takes place in the upper boundaries of the vortex system (Figure 2c,e). As explained and identified through Figure 4b, in the throat the temperature levels of the flow drops down almost to the surface temperature of the SC in the cases for $Re \leq 20$; thus, the ζ values of these cases do not show interpretable variations in the downstream region. However, those of the $Re = 30$ – 40 flows show notable variations, where the plot implies that the 10 mm downstream displacement is nearly sufficient to stabilize the thermal equilibrium in the complete spanwise direction ($x_{ds} = 10$ mm). The temperature contours of Figure 2d ($Re = 30$) illustrate matching results with these findings; however, the thermal instability of the $Re = 50$ flow can even be inspected at $x_{ds} \geq 10$ mm (Figure 2f).

The spanwise temperature gradient (dT/dy) plots further detail the local temperature variations. The significantly increasing temperature data in the projecting trajectory of the throat are in harmony with the high temperature gradients. As the projecting trajectory temperature values drop in the streamwise direction ($x_{ds} = 0$ → 10 mm), accompanying weaker gradients are as well evaluated in the computations. This evaluation can be identified through the maximum values of spanwise temperature gradient, where the figures are $(dT/dy)_{Max} = 53.7$ → 3.7 K/m ($x_{ds} = 0$ → 10 mm) and $(dT/dy)_{Max} = 6318.3$ → 813.4 K/m for flows with $Re = 10$ and $Re = 50$, respectively. These numbers as well point out the stronger thermal mechanisms in high Reynolds number cases. On the other hand, the augmenting thermal potential in the SC's line of action, more specifically in the mixing zone, results in irregular temperature distributions, especially in high Reynolds number cases ($Re \geq 30$, Figures 2d,f and 5b). The spanwise

thermal disturbances are most inspectable in the vortex driven region of $y = 0\text{--}15$ mm, where the ζ values show decrease trends in the spanwise direction ($y = 0\text{--}15$ mm). As a consequence, the corresponding temperature gradients put forward the drop of temperature values with the dT/dy trends having negative signs ($dT/dy < 0$). It should be noted that the downstream mixing region of the SC involves scientifically complex thermal structures; thus, the dT/dy variations for different Re cases do not follow Reynolds number based orders. The disordered attitude and the rapid variations of superior dT/dy values appear to trigger the thermal entropy generation rates mostly on a local scale.

3.3.3. Entropy Generation Characteristics

The downstream ($x_{ds} = 0\text{--}10$ mm) entropy generation values, in terms of frictional ($S''_{\Delta P}$) and thermal ($S''_{\Delta T}$) components, are displayed for various Reynolds numbers ($Re = 10\text{--}50$) in Figure 5c. The disturbances and the high gradient nature of the velocity (Figure 5a) and temperature (Figure 5b) fields significantly characterize the second-law mechanisms of the downstream domain. It can be inspected from the figure that, the most remarkable jumps both in $S''_{\Delta P}$ and $S''_{\Delta T}$ coincide with the extreme gradient locations of velocity (Figure 5a) and temperature (Figure 5b). Indeed, this outcome exactly coincides with the primary outputs of Nourollahi *et al.* [25]. On the other hand, being in harmony with the present findings, Kamish and Oztop [28] explained the decrease trends in thermal entropy generation values in channel flow in terms of the fall of temperature gradients at the identical locations. Results on entropy generation indicate that exergy destruction mostly grows with Reynolds number and decrease in the streamwise direction ($x_{ds} = 0\text{--}10$ mm) (Table 4). However, the comprehensive mixing in the region occupied by the vortex system ($x_{ds} \geq 0$ mm and $y = 0\text{--}15$ mm), causes asymmetric entropy distributions. Thus, the spanwise variations of $S''_{\Delta P}$ and $S''_{\Delta T}$ expose disorders from the point of the impact of Reynolds number. Besides, since the layout of the streamwise velocity characteristics (u/U_0) does not show significant deviations in the flow direction inside the vortex zone, the formation of $S''_{\Delta P}$ distributions in the spanwise direction (y), especially for $y = 0\text{--}0.015$ m, can mostly be associated with the development of v/U_0 profiles (Figure 5a) in the corresponding region. However, for the thermal part of the entropy generation, the almost stable appearance of the temperature values in the streamwise direction (Figure 5b) highlights the dominant impact of spanwise temperature gradients (dT/dy) on the thermal entropy generation ($S''_{\Delta T}$). As a consequence, the locations of maximum $S''_{\Delta T}$ (Figure 5c) exactly coincide with those of the peak spots of dT/dy (Figure 5b). On the other hand, computational investigations identified that frictional entropy generation values attain higher values on the back-surface ($x_{ds} = 0$ mm) of SC and on the duct wall ($y = 25$ mm), which can be enlightened by the comparably stronger velocity gradients in the considered regions. Besides, for the thermal component the prominent flow domain comes out to be the projecting trajectory of the throat. Such that the $S''_{\Delta T}$ variations produce maximums on the streamwise line of action of $y = 0.02$ m; the peaks can even be observed at the downstream section of $x_{ds} = 10$ mm. On the other hand, due to the extensive cooling ($\zeta = 0$) of the flow in the $Re = 10$ case (Figures 2b and 5b) the thermal activity decays comprehensively. The consequent outcome can be observed in Table 4 with the comparably low mean Bejan number of $Be_{Mean} = 0.941$ at $x_{ds} = 10$ mm. Similarly, Nourollahi *et al.* [25] evaluated excess thermal entropy generation values in Poiseuille-Benard channel flow, which result in Bejan numbers up to $Be \cong 0.9$.

Table 4. Downstream entropy generation parameters for various x_{ds} sections and Re cases.

	x_{ds} (mm)	Re = 10	Re = 20	Re = 30	Re = 40	Re = 50
$(S'''_{\Delta P})_{Mean}$ (W/m ³ K)	0	1.58×10^{-6}	6.30×10^{-6}	1.42×10^{-5}	2.51×10^{-5}	3.88×10^{-5}
		2.30×10^{-5}	9.26×10^{-5}	2.02×10^{-4}	3.41×10^{-4}	5.09×10^{-4}
	2	6.41×10^{-7}	2.56×10^{-6}	6.00×10^{-6}	1.12×10^{-5}	1.82×10^{-5}
		5.72×10^{-6}	2.24×10^{-5}	5.26×10^{-5}	9.98×10^{-5}	1.65×10^{-4}
	4	3.19×10^{-7}	1.39×10^{-6}	3.55×10^{-6}	7.13×10^{-6}	1.23×10^{-5}
$(S'''_{\Delta P})_{Max}$ (W/m ³ K)	4	2.29×10^{-6}	9.98×10^{-6}	2.63×10^{-5}	5.56×10^{-5}	9.94×10^{-5}
		7	1.12×10^{-7}	5.65×10^{-7}	1.68×10^{-6}	3.85×10^{-6}
	7	5.32×10^{-7}	2.76×10^{-6}	8.97×10^{-6}	2.32×10^{-5}	4.76×10^{-5}
		10	4.68×10^{-8}	2.64×10^{-7}	8.76×10^{-7}	2.25×10^{-6}
	10	1.53×10^{-7}	9.61×10^{-7}	3.75×10^{-6}	1.12×10^{-5}	2.53×10^{-5}
$(S'''_{\Delta T})_{Mean}$ (W/m ³ K)	0	3.43×10^{-5}	8.72×10^{-3}	0.076	0.267	0.570
		4.66×10^{-4}	0.118	1.020	3.370	6.710
	2	8.50×10^{-6}	0.003	0.027	0.109	0.259
		3.95×10^{-5}	0.013	0.147	0.621	1.480
	4	3.81×10^{-6}	1.36×10^{-3}	0.016	0.066	0.160
$(S'''_{\Delta T})_{Max}$ (W/m ³ K)	4	1.13×10^{-5}	4.66×10^{-3}	0.066	0.301	0.741
		7	1.57×10^{-6}	6.26×10^{-4}	0.008	0.032
	7	3.23×10^{-6}	1.51×10^{-3}	0.025	0.129	0.373
		10	7.80×10^{-7}	3.19×10^{-4}	0.004	0.016
	10	1.36×10^{-6}	6.56×10^{-4}	0.012	0.066	0.198
Be_{Mean}	0	0.974	0.999	1.000	0.999	0.999
		1.000	1.000	1.000	1.000	1.000
	2	0.956	0.998	0.999	0.999	0.999
		0.999	0.999	0.999	0.999	0.999
	4	0.945	0.998	0.999	0.999	0.999
Be_{Max}	4	0.999	0.999	0.999	0.999	0.999
		7	0.940	0.998	0.999	0.999
	7	0.994	1.000	1.000	0.999	0.999
		10	0.941	0.998	0.999	0.999
	10	0.982	0.999	0.999	0.999	0.999

4. Conclusions

For the strong blockage case of $\beta = 0.8$, steady regime continuity, Navier-Stokes and energy equations are simultaneously solved to computationally investigate the effects of Reynolds number on the energy and exergy characteristics of the upstream, throat and downstream domains of a square cylinder in confined flow. Results are presented and discussed in detail.

Analyses of energy characteristics identified the following primary issues:

In the upstream domain, as the flow approaches the SC ($x_{us} \rightarrow 0$ mm), the mean and maximum values of u/U_o and v/U_o data increase with higher Re for $x_{us} \leq 4$ mm. Besides, the flows with low Reynolds number are determined to be more sensible to heat transfer and temperature drop in the earlier sections of the upstream region ($x_{us} > 7$ mm). In the closer flow domains of the SC ($x_{us} \leq 4$ mm), the thermal texture of the higher Reynolds number cases are evaluated to be more motivated. Computations show that as the non-dimensional centerline temperature value drops from $\zeta = 0.585$

($x_{us} = 4$ mm) to $\zeta = 0.025$ ($x_{us} = 0$ mm) at $Re = 50$, those of the $Re = 10$ case are $\zeta = 0.281$ and $\zeta = 0.012$. In the throat, due to its strict guidance, the flow becomes fully developed rapidly ($x_{th} = 10$ mm), such that the spanwise motion vanishes ($v = 0$). The streamwise velocity values are computed to accelerate up to $u/U_0 = 6.381 \rightarrow 6.789$ ($Re = 10 \rightarrow 50$), where the maximum values are located exactly at the symmetry axis, verifying the fully developed character. At the exit section of the throat ($x_{th} \approx 40$ mm), the flow domain is intensely disturbed resulting in the emerging of spanwise velocities and deviations in the streamwise velocity profiles; moreover, the exit jets are persistently oriented towards the symmetry axis of the duct. Downstream of the SC, in the flow with $Re = 20$ the spanwise velocities turned out to become weaker in the downstream direction with negative spanwise velocity values at $x_{ds} = 7$ mm, indicating the completion of the recirculation zone. However, the strength of the vortex development in the $Re = 50$ flow is evident with the comparably advanced upward values of spanwise velocity, particularly in the $y = 0-0.020$ m region. In the line of action of the SC, the temperature values are computed to augment in the flow direction ($x_{ds} = 0 \rightarrow 10$ mm); but the reverse mechanism is set for the projecting trajectory of the throat.

Analyses of exergy characteristics resulted in the following main findings:

The most remarkable frictional entropy generation values in the upstream region are attained at the inlet section ($x_{us} = 0$ mm) of the throat, specifically on the corner of the SC ($y = 20$ mm), which is associated with the unguided mixing but also with the maximum accelerations recorded throughout the domain. Similar to the findings on $S_{\Delta P}'''$, the most remarkable ascents in $S_{\Delta T}'''$ are also located around the inlet corner of the SC ($x_{us} = 0$ mm and $y = 20$ mm). Towards the SC ($x_{us} = 10 \rightarrow 0$ mm) the centerline, ($y = 0$ mm) $S_{\Delta P}'''$ values continuously decrease, where the drops become significant for $x_{us} < 2$ mm; which can be associated with the deceleration of the streamwise velocity values at the centerline, which results in the completely stagnant flow on the front-surface of the SC ($x_{us} = 0$ mm & $y = 0$ mm). Within the throat, the frictional entropy generation values augment with Reynolds number. Additionally, the impact of Re on $S_{\Delta P}'''$ is observed to decrease in the flow direction inside the throat, with the $(S_{\Delta P}''')_{\text{Mean-}Re=50} / (S_{\Delta P}''')_{\text{Mean-}Re=10}$ ratios of 36.29 and 24.08 at $x_{th} = 0$ mm and $x_{th} = 40$ mm, respectively. Besides, the thermal entropy generation data figured out to decrease in a demanding manner in the streamwise direction for the complete Reynolds number range in the throat. Entropy generation in the downstream flow domain indicates that exergy destruction grows with Reynolds number and decrease in the streamwise direction ($x_{ds} = 0 \rightarrow 10$ mm). However, asymmetric entropy distributions, in the region occupied by the vortex system ($x_{ds} \geq 0$ mm and $y = 0-15$ mm), are identified which are consequences of the comprehensive mixing in the corresponding zone. The almost stable appearance of the downstream temperature values in the streamwise direction highlights the dominant impact of spanwise temperature gradients (dT/dy) on the thermal entropy generation ($S_{\Delta T}'''$). As a consequence, the locations of maximum $S_{\Delta T}'''$ (Figure 5c) exactly coincide with those of the peak spots of dT/dy .

Acknowledgements

The author would like to acknowledge the Scientific Research Projects Department of Uludag University for supporting this research under the project number of KUAP(MH) 2014/15.

Nomenclature

A	area (m ²)
B	edge of square cylinder (m)
Be	Bejan number
Br	Brinkman number
h	heat transfer coefficient (W/m ² K)
H	channel height (m)
\dot{m}	mass flow rate (kg/s)
N _s	entropy generation number
P	static pressure (Pa)
Pr	Prandtl number
R	gas constant (J/kgK)
Re	Reynolds number
S ^{'''}	local entropy generation (W/m ³ K)
t	time (s)
T	temperature (K)
u	streamwise velocity (m/s)
v	spanwise velocity (m/s)
U	core velocity (m/s)
x	streamwise distance (m)
y	spanwise distance (m)

Greek Symbols

α	thermal diffusivity (m ² /s)
β	blockage ratio
ζ	non-dimensional temperature
κ_f	thermal conductivity of fluid (W/mK)
μ	dynamic viscosity (Pa.s)
ρ	density (kg/m ³)
θ	non-dimensional temperature effect
τ	shear stress (Pa)

Subscripts

*	non-dimensional	∞	inlet
B	edge of square cylinder	c, s	centerline, surface
ch, th	channel, throat	cr	critical
ΔP	frictional	ΔT	thermal
o	mean	us, ds	upstream, downstream

References

1. Chakraborty, J.; Verma, N.; Chhabra, R.P. Wall effects in flow past a circular cylinder in a plane channel: A numerical study. *Chem. Eng. Process.* **2004**, *43*, 1529–1537.
2. Nirmalkar, N.; Chhabra, R.P.; Poole, R.J. Laminar forced convection heat transfer from a heated square cylinder in a Bingham plastic fluid. *Int. J. Heat Mass Transfer* **2013**, *56*, 625–639.
3. Rao, P.K.; Sahu, A.K.; Chhabra, R.P. Momentum and heat transfer from a square cylinder in power-law fluids. *Int. J. Heat Mass Transf.* **2011**, *54*, 390–403.
4. Dhiman, A.K.; Anjaiah, N.; Chhabra, R.P. Mixed convection from a heated square cylinder to Newtonian and power-law fluids. *J. Fluid Eng.* **2007**, *129*, 506–513.
5. Chen, X.; Yu, P.; Winoto, S.H. Numerical analysis for the flow past a porous square cylinder based on the stress-jump interfacial-conditions. *Int. J. Numer. Methods Heat Fluid Flow* **2008**, *18*, 635–655.
6. Sharma, A.; Eswaran, V. Heat and fluid flow across a square cylinder in the two-dimensional laminar flow regime. *Numer. Heat Transf. A* **2004**, *45*, 247–269.
7. Chatterjee, D.; Mondal, B. Effect of thermal buoyancy on vortex shedding behind a square cylinder in cross flow at low Reynolds numbers. *Int. J. Heat Mass Transf.* **2011**, *54*, 5262–5274.
8. Paliwal, B.; Sharma, A.; Chhabra, R.P. Power law fluid flow past a square cylinder: momentum and heat transfer characteristics. *Chem. Eng. Sci.* **2003**, *58*, 5315–5329.
9. Sen, S.; Mittal, S.; Biswas, G. Flow past a square cylinder at low Reynolds numbers. *Int. J. Numer. Methods Fluids* **2011**, *67*, 1160–1174.
10. Breuer, M.; Bernsdorf, J.; Zeiser, T. Accurate computations of the laminar flow past a square cylinder based on two different methods: Lattice-Boltzmann and finite-volume. *Int. J. Heat Fluid Flow* **2000**, *21*, 186–196.
11. Bouaziz, M.; Kessentini, S.; Turki, S. Numerical prediction of flow and heat transfer of power-law fluids in a plane channel with a built-in heated square cylinder. *Int. J. Heat Mass Transf.* **2010**, *53*, 5420–5429.
12. Dhiman, A.K.; Chhabra, R.P.; Eswaran, V. Steady mixed convection across a confined square cylinder. *Int. Commun. Heat Mass Transf.* **2008**, *35*, 47–55.
13. Rahnama, M.; Hadi-Moghaddam, H. Numerical investigation of convective heat transfer in unsteady laminar flow over a square cylinder in a channel. *Heat Transf. Eng.* **2005**, *26*, 21–29.
14. Dhiman, A.K.; Chhabra, R.P.; Eswaran, V. Steady flow across a confined square cylinder: Effects of power-law index and blockage ratio. *J. Non-Newton. Fluid Mech.* **2008**, *148*, 141–150.
15. Sharma, A.; Eswaran, V. Effect of channel confinement on the two-dimensional laminar flow and heat transfer across a square cylinder. *Numer. Heat Transf. A* **2005**, *47*, 79–107.
16. Chen, S. Analysis of entropy generation in counter-flow premixes hydrogen-air combustion. *Int. J. Hydrog. Energ.* **2010**, *35*, 1401–1411.
17. Granovskii, M.; Dincer, I.; Rosen, M.A. Application of oxygen ion-conductive membranes for simultaneous electricity and hydrogen generation. *Chem. Eng. J.* **2006**, *120*, 193–202.
18. Hooman, K.; Haji, S.A. Analysis of heat transfer and entropy generation for a thermally developing Brinkman-Brinkman forced convection problem in a rectangular duct with isoflux walls. *Int. J. Heat Mass Transf.* **2007**, *50*, 4180–4194.

19. Zimparov, V. Energy conservation through heat transfer enhancement techniques. *Int. J. Energy Res.* **2002**, *26*, 675–696.
20. Chen, S.; Du, R. Entropy generation of turbulent double-diffusive natural convection in a rectangular cavity. *Energy* **2011**, *36*, 1721–1734.
21. Rakshit, D.; Balaji, C. Thermodynamic optimization of conjugate convection from a finned channel using genetic algorithms. *Heat Mass Transf.* **2005**, *41*, 535–544.
22. Ko, T.H. Numerical investigation of laminar forced convection and entropy generation in a helical coil with constant wall heat flux. *Numer. Heat Transf. A* **2006**, *49*, 257–278.
23. Guo, J.; Xu, M.; Cheng, L. Second law analysis of curved rectangular channels. *Int. J. Therm. Sci.* **2011**, *50*, 760–768.
24. Makinde, O.D. Entropy-generation analysis for variable-viscosity channel flow with non-uniform wall temperature. *Appl. Energy* **2008**, *85*, 384–393.
25. Nourollahi, M.; Farhadi, M.; Sedighi, K. Numerical study of mixed convection and entropy generation in the Poiseuille-Benard channel in different angles. *Therm. Sci.* **2010**, *14*, 329–340.
26. Mahmud, S.; Fraser, R.A. Second-law analysis of forced convection in a circular duct for non-Newtonian fluids. *Energy* **2006**, *31*, 2226–2244.
27. Kurtbas, I.; Celik, N.; Dincer, I. Exergy transfer in a porous rectangular channel. *Energy* **2010**, *35*, 451–460.
28. Kamish, F.; Oztop, H.F. Second-law analysis of the 2D laminar flow of two-immiscible, incompressible viscous fluids in a channel. *Heat Mass Transf.* **2008**, *44*, 751–761.
29. Jarungthammachote, S. Entropy generation analysis for fully developed laminar convection in hexagonal duct subjected to constant heat flux. *Energy* **2010**, *35*, 5374–5379.
30. Andreozi, A.; Auletta, A.; Manca, O. Entropy generation in natural convection in a symmetrically and uniformly heated vertical channel. *Int. J. Heat Mass Transf.* **2006**, *49*, 3221–3228.
31. Kotas, T.J.; Mayhew, Y.R.; Raichura, R.C. Nomenclature for exergy analysis. *Proc. Inst. Mech. Eng. A* **1995**, *209*, 275–280.
32. Bianco, V.; Manca, O.; Nardini, S. Entropy generation analysis of turbulent convection flow of Al₂O₃-water nanofluid in a circular tube subjected to constant wall heat flux. *Energy Convers. Manag.* **2014**, *77*, 306–314.
33. Bianco, V.; Manca, O.; Nardini, S. Performance analysis of turbulent convection heat transfer of Al₂O₃-water nanofluid in circular tubes at constant wall temperature. *Energy* **2014**, *77*, 403–413.
34. Mkwizu, H.M.; Makinde, D.O. Entropy generation in a variable viscosity channel flow of nanofluids with convective cooling. *Comptes Rendus Mecanique* **2015**, *343*, 38–56.
35. Eegunjobi, S.A.; Makinde, D.O. Entropy generation analysis in transient variable viscosity couette flow between two concentric pipes. *J. Therm. Sci. Technol.* **2014**, *9*, doi:10.1299/jtst.2014jtst0008.
36. Incropera, F.P.; De Witt, D.P. *Fundamentals of Heat and Mass Transfer*; Wiley: New York, NY, USA, 1990.
37. White, F.M. *Viscous Fluid Flow*; McGraw-Hill: New York, NY, USA, 1991.
38. Bejan, A. *Entropy Generation through Heat and Fluid Flow*; Wiley: New York, NY, USA, 1982.
39. Bejan, A. *Advanced Engineering Thermodynamics*; Wiley: New York, NY, USA, 1988.

40. Abu-Nada, E. Entropy generation due to heat and fluid flow in backward facing step flow with various expansion ratios. *Int. J. Energy* **2006**, *3*, 419–435.
41. ANSYS CFX. *User Manual*; ANSYS: Canonsburg, PA, USA, 2005.
42. Farooji, E.V.; Bajestan, E.E.; Niazmand, H. Unconfined laminar nanofluid flow and heat transfer around a square cylinder. *Int. J. Heat Mass Transf.* **2012**, *55*, 1475–1485.
43. Dhiman, A.K.; Chhabra, R.P.; Sharma, A. Effects of Reynolds and Prandtl numbers on heat transfer across a square cylinder in the steady flow regime. *Numer. Heat Transf. A* **2006**, *49*, 717–731.

© 2015 by the authors; licensee MDPI, Basel, Switzerland. This article is an open access article distributed under the terms and conditions of the Creative Commons Attribution license (<http://creativecommons.org/licenses/by/4.0/>).